The Astrophysical Journal Letters, 975:L18 (9pp), 2024 November 1 https://doi.org/10.3847/2041-8213/ad85c9

The Cosmological Optical Convergence: Extragalactic Background Light from TeV Gamma Rays

Lucas Gréaux[1], Jonathan Biteau[1,2], and Mireia Nievas Rosillo[3,4]
[1] Université Paris-Saclay, CNRS/IN2P3, IJCLab, 91405 Orsay, France; lucas.greaux@gmail.com
[2] Institut Universitaire de France (IUF), France
[3] Instituto de Astrofísica de Canarias, E-38205 La Laguna, Tenerife, Spain
[4] Universidad de La Laguna, Dept. Astrofísica, E-38206 La Laguna, Tenerife, Spain
Received 2024 July 22; revised 2024 October 4; accepted 2024 October 9; published 2024 October 29

Abstract

The intensity of the extragalactic background (EBL), the accumulated optical and infrared emissions since the first stars, is the subject of a decades-long tension in the optical band. These photons form a target field that attenuates the γ-ray flux from extragalactic sources. This Letter reports the first γ-ray measurement of the EBL spectrum at $z = 0$ that is purely parametric and independent of EBL evolution with redshift over a wavelength range from 0.18 to 120 μm. Our method extracts the EBL absorption imprint on more than 260 archival TeV spectra from the STeVECat catalog by marginalizing nuisance parameters describing the intrinsic emission and instrumental uncertainties. We report an intensity at 600 nm of $6.9 \pm 1.9\,\mathrm{nW\,m^{-2}\,sr^{-1}} \times h_{70}$, which is indistinguishable from the intensity derived from integrated galaxy light (IGL) and compatible with direct measurements taken beyond Pluto's orbit. We exclude with 95% confidence diffuse contributions to the EBL with an intensity relative to the IGL, f_{diff}, greater than 20% and provide a measurement of the expansion rate of the Universe at $z = 0$, $H_0 = 67^{+7}_{-6}\,\mathrm{km\,s^{-1}\,Mpc^{-1}} \times (1 + f_{\mathrm{diff}})$, which is EBL-model independent. IGL, direct, and γ-ray measurements agree on the EBL intensity in the optical band, finally reaching a cosmological optical convergence.

Unified Astronomy Thesaurus concepts: Cosmic background radiation (317); Galaxy counts (588); Gamma-ray astronomy (628); Night sky brightness (1112); Observational cosmology (1146)

Materials only available in the online version of record: figure set

1. Introduction

The cumulative emission from all radiating sources since the birth of the first stars forms the extragalactic background light (EBL), which is second in intensity only to the cosmic microwave background (e.g., S. P. Driver 2021, for a review). The broadband spectrum of the EBL is dominated by the cosmic optical background (COB; 0.1–8 μm) and the cosmic infrared background (CIB; 8–1000 μm). The COB and CIB consist mainly of light either directly escaping from galaxies or absorbed by dust grains and thermally radiated. As a record of all photon production pathways since recombination, the EBL is a powerful cosmological probe and can help constrain physics beyond the Standard Model (see A. Cooray 2016; J. Biteau & M. Meyer 2022).

Current best estimates of the EBL intensity come from the combined emission from stars, dust, and the active nuclei of galaxies, called the integrated galaxy light (IGL). Based on measured light from resolved galaxies, IGL estimates currently reach a precision of 5%–20% (see S. P. Driver et al. 2016; S. Koushan et al. 2021) and provide only lower bounds on the EBL, omitting contribution from low-surface-brightness and subthreshold source populations. In contrast, direct measurements of the EBL, which determine the cumulative light emission from both diffuse and resolved sources, provide a comprehensive view of the background intensity at the cost of contamination by foreground emissions (K. Mattila & P. Väisänen 2019). Measurements from within the solar system must, for example, account for the zodiacal light foreground (diffuse reflection of sunlight on interplanetary dust; see M. G. Hauser & E. Dwek 2001), which outshines the EBL by more than 1 order of magnitude at one astronomical unit.

Any difference between direct and IGL measurements (e.g., R. A. Bernstein 2007; K. Kawara et al. 2017; S. Matsuura et al. 2017; T. R. Lauer et al. 2021, 2022; T. Symons et al. 2023), i.e., the so-called optical controversy in the visible band (S. P. Driver 2021), could be explained by unobserved faint galaxies (C. J. Conselice et al. 2016), by unresolved emissions from or around known galaxies (A. Cooray et al. 2012b; M. Zemcov et al. 2014; T. Matsumoto & K. Tsumura 2019), or by physics beyond the Standard Model (J. L. Bernal et al. 2022). However, observations from the Hubble Space Telescope seem to disfavor at least some of these explanations (D. M. Kramer et al. 2022; K. Nakayama & W. Yin 2022), and an excess with respect to the IGL may instead be associated with misunderstood foreground emissions. Recent analysis by M. Postman et al. (2024) of an extensive data set from the LORRI instrument aboard the New Horizons probe (A. F. Cheng et al. 2008; H. A. Weaver et al. 2020), beyond Pluto's orbit where zodiacal light is negligible, thus seems to suggest a misestimation of foreground emissions in earlier studies from the same team (T. R. Lauer et al. 2021, 2022).

In addition to direct and IGL measurements, the COB and CIB can be measured indirectly within observational γ-ray cosmology through their interactions with γ-rays. Predicted by A. I. Nikishov (1961) and R. J. Gould & G. P. Schreder (1967), observational constraints on the transparency of the Universe to γ-rays were first placed by F. W. Stecker et al. (1992). Two

decades later, the first measurements were made using the absorption patterns induced in the γ-ray spectra of extragalactic sources at high energies (HE; 0.1–300 GeV; M. Ackermann et al. 2012) and at very high energies (VHE; 0.1–30 TeV; H.E.S.S. Collaboration et al. 2013). However, the most recent EBL measurements using γ-ray data only (H.E.S.S. Collaboration et al. 2017; A. U. Abeysekara et al. 2019; V. A. Acciari et al. 2019; Z. Cao et al. 2023) lack the precision to resolve the controversy (see A. Domínguez et al. 2024, and references therein).

Following J. Biteau & D. A. Williams (2015) and A. Desai et al. (2019), we propose a new analysis method using a fully Bayesian framework, which we apply to the most comprehensive catalog of archival VHE observations to date, STeVECat (L. Gréaux et al. 2023a), and to contemporaneous HE observations from Fermi Large Area Telescope (LAT). This framework allows us to overcome the usual limitations of γ-ray analyses of EBL, which are related to the unknown spectra emitted by the sources (B. Biasuzzi et al. 2019) and to systematic uncertainties in the energy scale (see, e.g., H.E.S.S. Collaboration et al. 2013) of imaging atmospheric Cherenkov telescopes (IACTs). Our analysis also overcomes the limitations of the studies of J. Biteau & D. A. Williams (2015) and A. Desai et al. (2019), whose results are partially dependent on EBL evolution models (via a fixed redshift evolution parameter and the modeled metaobservable, respectively).

We adopt as a baseline a concordance ΛCDM model with $H_0 = 70\,\mathrm{km\,s^{-1}\,Mpc^{-1}}$, $\Omega_\mathrm{m} = 0.3$, and $\Omega_\Lambda = 0.7$. Uncertainties reported in this work correspond to 68% credible intervals.

2. Gamma-Ray Data Sets

2.1. VHE γ-Ray Data

We study spectra from jetted active galactic nuclei and long gamma-ray bursts published in peer-reviewed journals by ground-based γ-ray instruments from 1992 to 2021 and collected in STeVECat (L. Gréaux et al. 2023a, 2023b), the largest database of archival VHE spectra from extragalactic sources to date.[5] In STeVECat, each source is assigned a spectroscopic redshift measurement with a reliability flag from the literature review by P. Goldoni (2021). Most spectra come from the current generation of IACTs, H.E.S.S. (T. Ashton et al. 2020), MAGIC (J. Aleksić et al. 2016), and VERITAS (J. Holder et al. 2006), which observe few-degree patches of the extragalactic γ-ray sky down to $\sim$50 GeV and up to $\sim$20 TeV.

From STeVECat, we select nonredundant spectra with at least four flux points (excluding upper limits) from sources with a reliable redshift measurement at $z > 0.01$. At such a distance or below, substantial EBL absorption of γ-rays is only expected beyond 20 TeV (e.g., A. Saldana-Lopez et al. 2021). The threshold of four flux points per spectrum allows us to extract most of the EBL information from the γ-ray data without bias. Our selection amounts to 268 spectra from 45 extragalactic sources (see Appendix A), going up to redshift $z = 0.939$ (PKS 1441+25). To date, this is the most extensive VHE spectral corpus used for an EBL study: in their reference study, J. Biteau & D. A. Williams (2015) collected 86 spectra from 32 sources, up to redshift $z = 0.287$. Almost all sources in our data samples are jetted active galactic nuclei (mostly blazars), with the exception of three long γ-ray bursts.

[5] https://zenodo.org/records/8152245

2.2. HE γ-Ray Data

The LAT on board the Fermi Gamma Ray Space Telescope is a pair-conversion telescope continuously observing the sky in the γ-ray band from $\sim$100 MeV to more than 100 GeV (W. B. Atwood et al. 2009). As EBL absorption is negligible up to 100 GeV for sources with redshift $z < 1$ (e.g., A. Saldana-Lopez et al. 2021), Fermi-LAT provides a measurement of the nonattenuated part of the spectra of γ-ray sources listed in STeVECat. We analyzed Fermi-LAT events at energies between 100 MeV and 100 GeV with `Pass 8 SOURCE` class within a region of interest of 15 deg radius around each of the STeVECat sources. We considered a time integration window corresponding to the start and end date of the VHE observations, extended by including the 3 hr periods preceding and following the observation to ensure at least two HE snapshots of the selected region per contemporaneous STeVECat spectrum. This analysis results in 64 contemporaneous spectra.

The data were analyzed with the Fermi Science Tools (Fermi Science Support Development Team 2019) through the high-level wrapper `enrico` (D. Sanchez & C. Deil 2015). We used the latest available version of the instrument response functions (`P8R3_SOURCE_V3`), setting the recommended zenith cuts of 90 deg to avoid Earth's limb contamination, and `DATA_QUAL==1 && LAT_CONFIG==1` to preserve only good-quality data. We modeled the isotropic and Galactic diffuse background using the models tabulated in `iso_P8R3_SOURCE_V3_v1.txt` and `gll_iem_v07.fits`, respectively. For each analysis, we simultaneously modeled all sources from the Fermi-LAT 12 Yr Point Source Catalog (4FGL-DR3, S. Abdollahi et al. 2022) within 20 deg of the target VHE source. The position and extension of all sources in the sky were kept frozen to the catalog values, and we only left the normalization free for very bright sources (significance above 40σ) in the region. For the target source, we adopted a log-parabola spectral model, setting hard limits between -2 and 2 on the spectral curvature term, to be consistent with the treatment described in Section 3.

We show in Figure 1 an exemplary spectrum used in this study, corresponding to an observation of the source 1ES 1011+496 by the MAGIC telescopes and a contemporaneous Fermi-LAT spectrum, shown as a dashed confidence band in the inset. We use the spectral indices and curvatures reconstructed at HE as well their statistical uncertainties to establish the Bayesian priors on the intrinsic shape of the source spectra, as described in the next section. While we assume no differential spectral shape evolution between HE and VHE samples, we do not assume that the HE flux level corresponds to the VHE flux, as blazars can exhibit large-amplitude variability on time scales as short as a few minutes (F. Aharonian et al. 2007). An overall good match is found a posteriori between HE and VHE flux normalizations.

3. Analysis Framework

3.1. Spectral Model

The spectra emitted by VHE sources, before EBL absorption, are unknown and must be modeled. They are best reproduced by power laws with or without intrinsic curvature and energy cutoff (e.g., J. Biteau & D. A. Williams 2015). The presence or absence of these spectral features can affect the reconstruction of the EBL in a frequentist framework

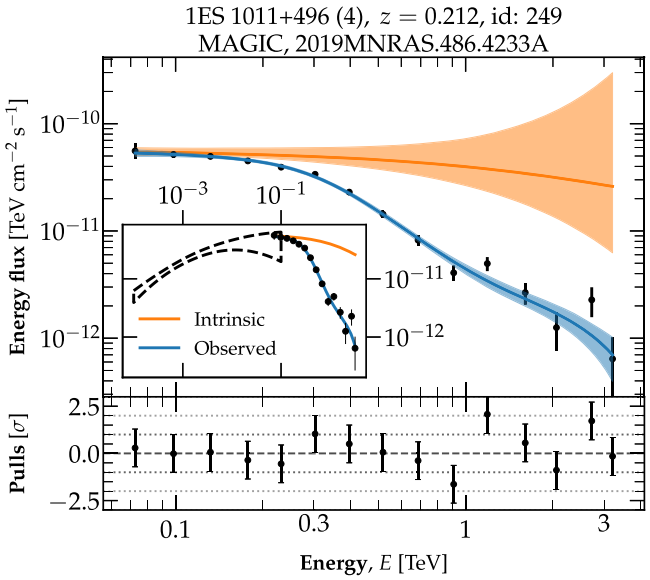

Figure 1. Top: spectrum of the source 1ES 1011+496 observed between MJD 56694 and MJD 56723. The black points correspond to the MAGIC observation (SAO/NASA ADS reference 2019MNRAS.486.4233A), and the dashed black confidence band in the inset corresponds to the contemporaneous Fermi-LAT observation. The blue curve displays the reconstructed observed spectrum and the orange curve the reconstructed intrinsic spectrum. The main panel covers the VHE range, while the inset covers both HE and VHE ranges. Both data sets are compatible within 0.6σ at the geometric mean of the maximal HE and minimal VHE energy. Bottom: pulls, i.e., residuals normalized to the uncertainties, for the best reconstructed spectrum.
(The complete figure set (268 images) is available in the online article.)

(B. Biasuzzi et al. 2019). We overcome this difficulty by marginalizing over the intrinsic spectral parameters in a Bayesian framework.

We model the intrinsic spectra with the general model including both curvature and energy cutoff, a log-parabola with exponential cutoff (ELP):

$$\Phi_{\rm ELP}(E) = \Phi_0 \times e^{\eta - \Gamma \log(E/E_0) - \beta \log^2(E/E_0) - \lambda E}, \quad (1)$$

where E_0 and Φ_0 are fixed parameters defining a reference energy and flux. For a VHE spectrum with energy bounds $E_{\rm min}$ and $E_{\rm max}$, we take $E_0 = \sqrt{E_{\rm min} E_{\rm max}}$ and set Φ_0 as the geometric mean of the unattenuated flux at $E_{\rm min}$ and $E_{\rm max}$, using the reference attenuation from A. Saldana-Lopez et al. (2021). The logarithmic normalization η, index Γ, curvature β, and inverse cutoff λ are left free to vary for each spectrum.

We account for the potential bias in the energy reconstruction of VHE observatories using an energy-scale parameter $\varepsilon = \log(E/\tilde{E})$, where E is the observed energy of an event with true energy $\tilde{E}$. The joint analysis of HE and VHE spectra from the Crab Nebula yields values $-0.1 \lesssim \varepsilon \lesssim 0.1$ for different IACTs (C. Nigro et al. 2019). We model a differential spectrum observed at Earth, emitted at redshift z, by

$$\Phi(E, z) = e^{-\tau(\tilde{E}, z)} \times \Phi_{\rm ELP}(\tilde{E}). \quad (2)$$

The intrinsic spectral model of an observation k has five free parameters, which we write $\theta_k \equiv \{\eta_k, \Gamma_k, \beta_k, \lambda_k, \varepsilon_k\}$. We write $\Theta \equiv \{\theta_k\}_k$.

3.2. EBL Absorption

The EBL-induced attenuation of the γ-ray flux observed at energy E and emitted at redshift z is characterized by the optical depth, integrated over redshift $z' \leqslant z$, comoving EBL photon energy ϵ', and comoving angle between momenta $\mu' = 1 - \cos\theta'$:

$$\tau(E, z) = \int_0^z dz' \frac{\partial L}{\partial z'}(z') \int_0^\infty d\epsilon' \frac{4\pi}{c} \frac{\nu I_\nu(\epsilon', z')}{\epsilon'^2} \times \int_{-1}^1 d\mu' \frac{1-\mu'}{2} \sigma_{\gamma\gamma}(E(1+z'), \epsilon', \mu'), \quad (3)$$

where νI_ν is the EBL specific intensity and $\sigma_{\gamma\gamma}$ is the Breit–Wheeler cross section (see e.g., J. Biteau & D. A. Williams 2015). For a flat ΛCDM cosmology, the distance element is $\partial L/\partial z = c/H_0 \times (1+z)^{-1} \times (\Omega_\Lambda + \Omega_{\rm m}(1+z)^3)^{-1/2}$.

We parameterize the EBL redshift evolution as $\nu I_\nu(\epsilon', z') = \nu I_\nu(\epsilon, 0) \times (1+z')^{4-f_{\rm evol}}$, where $\epsilon = \epsilon'/(1+z')$ is the EBL photon energy at $z = 0$. Values of $f_{\rm evol}$ ranging from 1.2 to 1.7 have been showed by M. Raue & D. Mazin (2008) and J. Biteau & D. A. Williams (2015) to be compatible with the EBL evolution as modeled by T. M. Kneiske et al. (2002), A. Franceschini et al. (2008), and R. C. Gilmore et al. (2012). In this work, we marginalize over the nuisance parameter $f_{\rm evol}$ ranging from 1 to 2 to ensure the independence of the results from the choice of a specific EBL model.

Following J. Biteau & D. A. Williams (2015), we parameterize the EBL spectrum at $z = 0$ as a sum of Gaussian functions of $l = \ln(\lambda/\lambda_{\rm ref})$, with fixed means $(l_i)_i$ and deviation σ, leaving the amplitudes $(a_i)_i$ free to vary:

$$\nu I_\nu(l) = \sum_i a_i \exp\left(-\frac{(l-l_i)^2}{2\sigma^2}\right). \quad (4)$$

We impose that the sum of two successive Gaussians of unity amplitude is equal to one in between their means, i.e., $l_{i+1} - l_i = \sigma \times 2\sqrt{2\ln 2}$. The optical depth can be written as $\tau(E, z) = \sum_i a_i t_i(E, z)$, where the $t_i(E, z)$ are weights independent of the parameterization $(a_i)_i$ that can be computed in advance using the analytic kernel from J. Biteau & D. A. Williams (2015).

We chose the means l_i and deviation σ to fully cover the 400–900 nm band of the LORRI instrument aboard New Horizons: a Gaussian is centered around $\lambda_{\rm ref} = 600$ nm, with $\sigma/\ln 10 = 0.15$ dex. We model the EBL with eight Gaussians centered at wavelengths ranging from 300 nm to 80 μm based on the expected reach of STeVECat. Adding Gaussians at shorter or longer wavelengths has no impact on our results. This modeling of the EBL has nine parameters, which we write as $a = \{\{a_i\}_i, f_{\rm evol}\}$.

3.3. Bayesian Analysis

We search for the EBL parameters a that best describe the data set $\mathcal{D} = \{D_k\}_k$ of independent observations k using the model from Equation (2). The Gaussian likelihood $\mathcal{L} \propto \Pr(D_k | a, \theta_k)$ quantifies the deviation between the data D_k and the model of the flux:

$$\log \mathcal{L}(a, \theta_k) = -\frac{1}{2} \sum_{i \in D_k} \left(\frac{\Phi(E_i, z; a, \theta_k) - \Phi_i}{\sigma_i} \right)^2, \quad (5)$$

where $\Phi_i \pm \sigma_i$ is the flux observed at energy E_i.

This equation has 14 free parameters. With a median count of 7.5 flux points per spectrum, a frequentist method could face the problem of overfitting. In the Bayesian formulation, we

reconstruct the posterior distribution for each spectrum:

$$\Pr(a, \theta_k|D_k) = \frac{\mathcal{L}(a, \theta_k)\pi(a)\pi(\theta_k)}{\int \mathrm{d}a\, \mathrm{d}\theta_k\, \mathcal{L}(a, \theta_k)\pi(a)\pi(\theta_k)}, \quad (6)$$

where $\pi(a) = \Pr(a)$ and $\pi(\theta_k) = \Pr(\theta_k)$ are the priors on the EBL and spectral parameters, respectively.

We chose weakly informative priors to minimize the a priori knowledge on the expected EBL and spectral shape. In the $\log\Phi - \log E$ space, Equation (1) is linear in parameters η, Γ, β, and λ, and we consider uniform priors centered on their expected values (0, 2, 0, and 0, respectively). Negative values of β and λ may not be physical, but they must be allowed in order to preserve reconstruction symmetry around 0. We have confirmed through simulations that priors on these intrinsic parameters that are nonuniform or limited to positive values can lead to substantial biases in the reconstructed EBL intensities. When contemporaneous GeV data are available, we replace the priors on Γ and β with a bivariate Gaussian distribution based on the Fermi-LAT best-fit parameters and covariance (Section 2.2). We adopt a Gaussian prior on the energy-scale parameter ε between -0.3 and 0.3 with mean 0 and standard deviation 0.1 (see Section 3.1) and a uniform prior on the EBL evolution parameter $f_{\rm evol}$ between 1 and 2 (see Section 3.2). For each EBL normalization a_i, we consider a log-uniform prior between a tenth and 10 times the intensity predicted by A. Saldana-Lopez et al. (2021). The results are robust to reasonable changes in EBL priors, e.g., using a uniform instead of log-uniform prior on a_i.

We use the Markov Chain Monte Carlo implementation `emcee` (D. Foreman-Mackey et al. 2013) to sample the posterior distribution $\Pr(a, \theta_k|D_k)$ for each observation k. Using Bayes' formula, the independence of the observations, and marginalizing over θ_k, the posterior distribution $\Pr(a|\mathcal{D})$ can be written as

$$\frac{\Pr(a|\mathcal{D})}{\pi(a)} = \prod_k \int d\theta_k \frac{\Pr(a, \theta_k|D_k)}{\pi(a)}. \quad (7)$$

We compute the univariate distribution $\Pr(a_i|\mathcal{D}) = \int df_{\rm evol} \prod_{j\neq i} da_j \Pr(a|\mathcal{D})$ as the product of the univariate distribution $\Pr(a_i|D_k)$ for each spectrum k as per Equation (7), from which we extract the mean value and variance of a_i. Similarly, we compute the covariance between a_i and a_j from the bivariate distribution $\Pr(a_i, a_j|\mathcal{D})$ given the means and variances from the univariate distributions.

4. Results and Discussion

4.1. Reconstructed EBL Intensity

We applied the framework developed in Section 3.3 to the data presented in Section 2, choosing the `emcee` parameters to ensure the production of 10,000 independent samples. The reconstructed spectra are shown in Figure Set 1. We find a good match between the spectra and contemporaneous GeV data and report in Appendix B the compatibility between HE and VHE spectra.[6] The reconstructed intrinsic spectra are consistent with the expectations of the underlying astrophysical models, showing no detectable upward curvature or exponential increase.

[6] Over 64 spectra, only 2 present a tension at more than the 3σ level, which can be attributed to a misrepresentation of the source variability between the time-integrated GeV data and the discrete TeV observation segments.

The EBL specific intensity at $z = 0$ resulting from the posterior distribution $\Pr(a|\mathcal{D})$ in Equation (7) is shown in Figure 2, where the linear scale allows for more accurate comparisons with the IGL measurements than the logarithmic scale employed in previous studies. The values and correlation coefficients of the reconstructed EBL intensities are given in Appendix C. Variations on the reconstruction method of $\Pr(a|\mathcal{D})$ from the individual samples have a negligible impact on the EBL reconstruction. Similarly, fixing the energy-scale parameter or the EBL evolution, removing the HE prior, and removing the highest-energy flux point of each spectrum have minimal effect. Study of simulated data, to be presented in a forthcoming publication, suggests a bias smaller than 0.4 nW m^{-2} sr^{-1}, which is 2 to 3 times smaller than the reported uncertainties. These uncertainties take full account of the statistical uncertainties and energy-scale bias of γ-ray spectral measurements, as well as the uncertainty in the intrinsic spectrum underlying each observation.

We obtain relative uncertainties on the EBL intensity of around 12% between 1 and 5 μm and lower than 35% between 0.4 and 120 μm. The bluest wavelength bin is less constrained: EBL photons at 300 nm only induce substantial absorption of γ-rays for sources at $z > 2$, well beyond the range covered by STeVECat. Most of the spectral corpus comes from relatively nearby sources at $z \leqslant 0.2$, which precludes placing tight constraints on the EBL evolution with redshift.

Our measurement is compatible with recent γ-ray attenuation measurements based either on a scaled EBL model (e.g., V. A. Acciari et al. 2019; Z. Cao et al. 2023) or on a parameterization of the EBL spectrum (e.g., H.E.S.S. Collaboration et al. 2017; Fermi-LAT Collaboration 2018; A. U. Abeysekara et al. 2019). Our measurement is as precise as or more precise than previous VHE measurements over the entire wavelength range, even when compared to (probably less accurate) approaches that rely heavily on EBL models. Our measurement is not competitive with the HE measurement by Fermi-LAT Collaboration (2018) below 400 nm, as expected from VHE γ-ray sources at $z < 1$, but it does establish reference measurements based on γ-ray attenuation at longer wavelengths up to 120 μm. We do not propose a joint measurement including information from the IGL as in J. Biteau & D. A. Williams (2015) and A. Desai et al. (2019) but instead constrain the unresolved components of the EBL in the following.

4.2. Unresolved EBL Components

The indirect γ-ray measurements shown in Figure 2 appear to be in good agreement with the IGL measurements and with the models that aim to reproduce them (R. C. Gilmore et al. 2012; S. K. Andrews et al. 2017a; A. Saldana-Lopez et al. 2021).[7] In particular, the IGL measurement from S. Koushan et al. (2021) interpolated at 600 nm, $\nu I_\nu^{\rm IGL}(0.6\ \mu\mathrm{m}) = 7.6 \pm 0.3$ nW m^{-2} sr^{-1}, can be compared to the EBL intensity inferred from γ-ray data, $\nu I_\nu^{\gamma}(0.6\ \mu\mathrm{m}) = 6.9 \pm 1.9$ nW m^{-2} sr^{-1} $\times\, h_{70}$, where $h_{70} = H_0/70$ km s^{-1} Mpc^{-1}.

We present in Figure 3 the residual EBL intensity with respect to IGL measurements, compared to the residual intensity from New Horizons as determined in T. R. Lauer et al. (2022) and M. Postman et al. (2024). Our measurement at

[7] A comparative study of the models and their impact on astroparticle propagation will be presented in a subsequent publication.

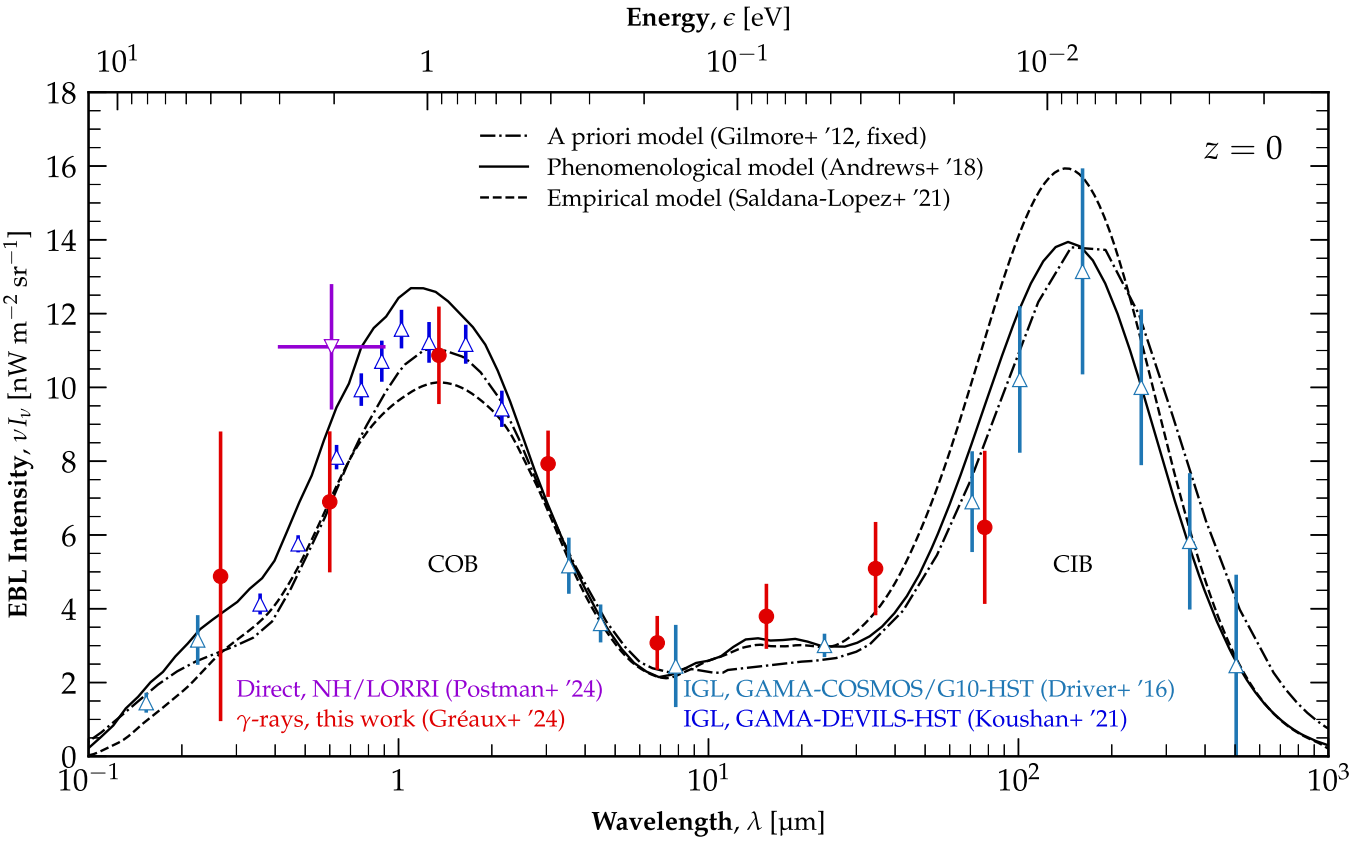

Figure 2. EBL intensity at $z = 0$ as a function of wavelength. Indirect γ-ray measurements from this work are shown as red circles. IGL measurements from S. P. Driver et al. (2016) and S. Koushan et al. (2021) are shown as upward-pointing triangles, as labeled in the figure. The direct measurement from M. Postman et al. (2024) in the optical band is shown as downward-pointing triangle. The EBL models from R. C. Gilmore et al. (2012), S. K. Andrews et al. (2017b), and A. Saldana-Lopez et al. (2021) are shown as dashed–dotted, solid, and dashed lines, respectively. These data sets are collected in J. Biteau (2023).

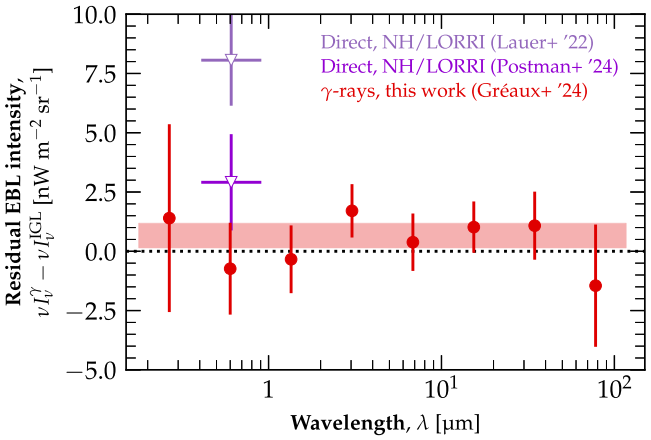

Figure 3. Residual EBL intensity at $z = 0$ as a function of wavelength with respect to the IGL measurements from S. P. Driver et al. (2016) and S. Koushan et al. (2021). Results derived in this work are shown with circles for each wavelength bin. The horizontal band is the result of a constant fit to the residuals over the full wavelength range. The measurements from T. R. Lauer et al. (2022) and M. Postman et al. (2024) are shown with downward-pointing triangles, as labeled in the figure.

600 nm rules out an excess with respect to IGL larger than 2.5 nW m^{-2} sr^{-1} at 95% confidence level. This result is consistent with the reanalysis of data from New Horizons by M. Postman et al. (2024), which found a COB level consistent with IGL inferences. The agreement between IGL and γ-ray data strongly suggests a foreground misestimation in studies such as R. A. Bernstein (2007), K. Kawara et al. (2017), S. Matsuura et al. (2017), and T. Symons et al. (2023). At wavelengths between 0.9 and 50 μm, we can exclude residual specific intensities greater than 3.6 nW m^{-2} sr^{-1} at 95% confidence level. This value remains 1 order of magnitude above the expected peak intensity of the relic emission from reionization sources (A. Cooray et al. 2012a).

No significant excess is found between γ-ray and IGL measurements at any wavelength. The average excess between 200 nm and 120 μm, $\langle \nu I_\nu^\gamma - \nu I_\nu^{\rm IGL} \rangle = 0.7 \pm 0.5$ nW m^{-2} sr^{-1}, sets a limit on the fraction of non-IGL contribution to the EBL. Assuming that diffuse, unresolved components contribute to the EBL with a spectrum similar to that of IGL and with a relative intensity $f_{\rm diff}$, i.e., $\nu I_\nu = \nu I_\nu^{\rm IGL} \times (1 + f_{\rm diff})$, we exclude at 95% confidence level values of $f_{\rm diff}$ greater than 20%. This upper limit constrains the amount of intra-halo light, whose contribution to the EBL has been estimated between 5% and 30% in the near-infrared (Y.-T. Cheng et al. 2021; S. P. Driver et al. 2022).

4.3. Hubble Constant

The propagation of VHE γ-rays can be used to measure the expansion rate of the Universe (A. Domínguez & F. Prada 2013; J. Biteau & D. A. Williams 2015; A. Domínguez et al. 2019; A. Domínguez et al. 2024). Fixing the optical depth τ in Equation (3) to the value inferred from γ-ray data determines the value of $\nu I_\nu / H_0$. The ratio of the indirect EBL measurement from γ-ray data to the IGL measurement thus reads $\nu I_\nu^\gamma / \nu I_\nu^{\rm IGL} = (1 + f_{\rm diff})/h_{70}$. The IGL intensity is

independent of the Hubble constant, as it is determined from the integral of an observed flux distribution.

Using the IGL measurements as Gaussian priors on the local intensity of the EBL, we leave the ratio $\nu I_\nu^\gamma / \nu I_\nu^{\rm IGL}$ free and reconstruct $H_0 = 67^{+7}_{-6}\,{\rm km\,s^{-1}\,Mpc^{-1}} \times (1 + f_{\rm diff})$, which is compatible with both the estimates based on cosmic microwave background observations (Planck Collaboration 2020) and the cosmic distance ladder (A. G. Riess et al. 2022). Although our uncertainties are about twice as large as those derived by A. Domínguez et al. (2024), our measurement is independent of any model of luminosity functions of galaxies contributing to the IGL at different redshifts.

A relevant and model-independent answer to the Hubble tension that makes use of this technique will require more precise measurements of the diffuse components of the EBL and of extragalactic γ-ray spectra.

5. Summary and Conclusion

After over a decade of tension, estimates of the EBL based on galaxy surveys and direct measurements are converging in the optical band. We present the first fully model-independent broadband spectrum of the EBL obtained from γ-ray measurements. We used archival observations from the current generation of IACTs collected in STeVECat (L. Gréaux et al. 2023a) and contemporaneous Fermi-LAT observations, which correspond to more than 3 times as many VHE spectra as used by previous γ-ray studies (J. Biteau & D. A. Williams 2015; A. Desai et al. 2019). We developed a fully Bayesian framework, which allows to circumvent the need for additional hypotheses on the emitted VHE spectra and to marginalize over the redshift evolution of the EBL as well as over systematic uncertainties of instrumental origin.

This indirect measurement of the EBL intensity is independent of both IGL and direct measurements. We report an intensity at 600 nm of $6.9 \pm 1.9\,{\rm nW\,m^{-2}\,sr^{-1}} \times h_{70}$, which is indistinguishable from the IGL measurement by S. Koushan et al. (2021) and compatible with the direct measurement from New Horizons (M. Postman et al. 2024). IGL, direct, and γ-ray measurements agree on the EBL intensity in the optical band, finally reaching a cosmological optical convergence. The excellent agreement between the γ-ray indirect measurement and the IGL measurement over nearly three decades in wavelength leaves little room for diffuse or unresolved contributions, $f_{\rm diff} < 20\%$, and provides a measurement on the expansion rate of the Universe at $H_0 = 67^{+7}_{-6}\,{\rm km\,s^{-1}\,Mpc^{-1}} \times (1 + f_{\rm diff})$. This measurement of the Hubble constant is independent of models of evolution of the EBL and its sources.

This work is focused on the EBL and Hubble parameter at $z = 0$. A combined analysis of the present sample with γ-ray data from sources at redshifts $z > 1$ observed by Fermi-LAT could yield better constraints on other cosmological parameters such as $\Omega_{\rm m}$ (A. Domínguez et al. 2024) and on the cosmic evolution of the EBL (S. K. Andrews et al. 2017b), which is closely linked to the cosmic star formation history (Fermi-LAT Collaboration 2018).

Significant advances in this scientific field are also expected from other observatories already in operation or about to become operational. Direct EBL measurements will benefit from a better understanding of foregrounds derived from observations by the Hubble Space Telescope (R. A. Windhorst et al. 2022) and the James Webb Space Telescope (R. A. Windhorst et al. 2023), not to mention the constraints on reionization sources from the latter. The galaxy counts from the large surveys by Euclid (see Euclid Collaboration 2024) and Vera C. Rubin Observatory (see Ž. Ivezić et al. 2019) may bring the accuracy of IGL measurements down to the percent level. The deployment of the Cherenkov Telescope Array Observatory (see CTA Consortium 2021) will finally provide unprecedented γ-ray spectral measurements in the TeV energy range. The stage is set for the precise measurements of the emission of all stars and galaxies since recombination.

Acknowledgments

We thank the reviewer for the constructive comments that helped to improve the quality of this Letter. We are also grateful to the colleagues who kindly provided comments on this Letter, in particular Tod Lauer. We gratefully acknowledge funding from ANR via the grant MICRO, ANR-20-CE92-0052. M.N.R. acknowledges support from the Agencia Estatal de Investigación del Ministerio de Ciencia, Innovación y Universidades (MCIU/AEI) under grant PARTICIPACIÓN DEL IAC EN EL EXPERIMENTO AMS and the European Regional Development Fund (ERDF) with reference PID2022-137810NB-C22 / DIO 10.13039/501100011033.

Appendix A
Gamma-Ray Sources

We present in Table 1 the list of extragalactic VHE sources that have been considered in this study. We provide the commonly used name and 4FGL name of each source, its class, its redshift, its Galactic longitude and latitude, and the number of associated VHE spectra. The information from Table 1 has been extracted from STeVECat (see L. Gréaux et al. 2023a). Most redshifts are spectroscopic estimates from the review of P. Goldoni (2021). The STeVECat identifier of each spectrum

Table 1
Sources Used in This Study

Source Name	4FGL Name	Class	Redshift	Galactic Coordinates (deg)		Spectra
				Longitude	Latitude	#
NGC 1275	J0319.8+4130	FR-I	0.018	150.58	−13.26	4
IC 310	J0316.8+4120	AGN	0.019	150.18	−13.73	8
3C 264	J1144.9+1937	FR-I	0.022	235.73	73.04	1
Mkn 421	J1104.4+3812	HBL	0.030	179.83	65.03	68
Mkn 501	J1653.8+3945	HBL	0.033	63.60	38.86	68
1ES 2344+514	J2347.0+5141	HBL	0.044	112.89	−9.91	5
Mkn 180	J1136.4+7009	HBL	0.045	131.91	45.64	1
1ES 1959+650	J2000.0+6508	HBL	0.047	98.00	17.67	17

Table 1
(Continued)

Source Name	4FGL Name	Class	Redshift	Galactic Coordinates (deg)		Spectra
				Longitude	Latitude	#
AP Librae	J1517.7−2422	LBL	0.048	340.68	27.58	1
PKS 0625−354	J0627.0−3529	AGN	0.055	243.45	−19.97	1
I Zw 187	J1728.3+5013	HBL	0.055	77.07	33.54	2
NVSS J073326+515355	J0733.4+5152	EHBL	0.065	166.00	27.32	1
BL Lacertae	J2202.7+4216	IBL	0.069	92.59	−10.44	5
PKS 2005−489	J2009.4−4849	HBL	0.071	350.37	−32.60	5
GRB 190829A	⋯	LGRB	0.079	187.68	−54.99	2
PMN J0152+0146	J0152.6+0147	HBL	0.080	152.38	−57.54	1
S3 1741+19	J1744.0+1935	HBL	0.084	43.84	23.34	1
W Comae	J1221.5+2814	IBL	0.102	201.74	83.29	2
MS 13121−4221	J1315.0−4236	HBL	0.105	307.55	20.05	1
PKS 2155−304	J2158.8−3013	HBL	0.116	17.73	−52.25	16
B3 2247+381	J2250.0+3825	HBL	0.119	98.25	−18.58	1
1H 0658+595	J0710.4+5908	EHBL	0.125	157.40	25.43	1
H 1426+428	J1428.5+4240	EHBL	0.129	77.49	64.90	3
B2 1215+30	J1217.9+3007	HBL	0.130	188.87	82.05	9
1ES 0806+524	J0809.8+5218	HBL	0.138	166.25	32.91	3
PKS 1440−389	J1443.9−3908	HBL	0.139	325.64	18.71	1
1ES 0229+200	J0232.8+2018	EHBL	0.139	152.94	−36.61	4
1RXS J101015.9−311909	J1010.2−3119	HBL	0.143	266.91	20.05	1
1ES 1440+122	J1442.7+1200	HBL	0.163	8.33	59.84	1
H 2356−309	J2359.0−3038	EHBL	0.165	12.84	−78.04	3
MG4 J200112+4352	⋯	HBL	0.174	79.07	7.11	1
RX J0648.7+1516	J0648.7+1516	HBL	0.179	198.99	6.33	1
PG 1218+304	J1221.3+3010	EHBL	0.184	186.36	82.73	3
1ES 1101−232	J1103.6−2329	EHBL	0.186	273.19	33.08	1
1ES 0347−121	J0349.4−1159	EHBL	0.188	201.93	−45.71	1
1E 0317.0+1835	J0319.8+1845	HBL	0.190	165.11	−31.70	1
1ES 1011+496	J1015.0+4926	HBL	0.212	165.53	52.71	4
1ES 0414+009	J0416.9+0105	EHBL	0.287	191.81	−33.16	2
PKS 1510−089	J1512.8−0906	FSRQ	0.360	351.29	40.14	5
GRB 190114C	⋯	LGRB	0.424	222.47	−53.08	5
4C +21.35	J1224.9+2122	FSRQ	0.434	255.07	81.66	1
3C 279	J1256.1−0547	FSRQ	0.536	305.10	57.06	1
GRB 180720B	⋯	LGRB	0.654	94.84	−63.07	1
B2 1420+32	J1422.3+3223	FSRQ	0.682	53.35	69.59	1
PKS 1441+25	J1443.9+2501	FSRQ	0.939	34.56	64.70	3

Note. The third column provides the object class. LGRB stands for long-duration gamma-ray burst, FR-I for radio galaxy of Fanaroff–Riley Type 1, AGN for active galactic nucleus of unknown subclass, FSRQ for flat-spectrum radio quasar. LBL, IBL, HBL, and EHBL stand for low-, intermediate-, high-, and extremely high-synchrotron peak BL Lac, respectively.

and the corresponding bibliographic reference can be found in Figure Set 1.

Appendix B
Compatibility Between GeV Data and TeV Reconstruction

We present in Table 2 the list of spectra for which a contemporaneous Fermi-LAT observation has been considered in this study. We provide the global and per-source identifiers of each spectrum, the commonly used name and 4FGL name of the corresponding source, the Fermi-LAT observation period considered and corresponding livetime, and the tension between the GeV data and the TeV reconstruction at the midpoint of the HE and VHE energy bands.

Table 2
Spectra with Contemporaneous Fermi-LAT Observations

Spectrum Id.	Source Name	4FGL Name	Observation Period	HE Livetime (hr)	$\sigma_{\mathrm{HE,VHE}}$
1 (1)	NGC 1275	J0319.8+4130	55043.875–56992.125	46758	0.0
2 (2)	NGC 1275	J0319.8+4130	57631.875–57813.125	4350	1.4
3 (3)	NGC 1275	J0319.8+4130	57753.775–57754.205	10	0.2
4 (4)	NGC 1275	J0319.8+4130	57754.765–57756.155	33	0.3
5 (1)	IC 310	J0316.8+4120	55122.875–55241.125	2838	2.0
51 (38)	Mkn 421	J1104.4+3812	54849.875–54983.125	3198	0.6
55 (42)	Mkn 421	J1104.4+3812	56307.131–56307.408	7	0.0
57 (44)	Mkn 421	J1104.4+3812	56312.047–56312.379	8	0.0
58 (45)	Mkn 421	J1104.4+3812	56334.955–56335.285	8	0.0
74 (61)	Mkn 421	J1104.4+3812	56776.015–56776.455	11	0.3
76 (63)	Mkn 421	J1104.4+3812	57756.894–57757.406	12	>5
77 (64)	Mkn 421	J1104.4+3812	57784.877–57785.265	9	0.0
78 (65)	Mkn 421	J1104.4+3812	57787.914–57788.192	7	0.0
79 (66)	Mkn 421	J1104.4+3812	57788.900–57789.224	8	1.0
102 (21)	Mkn 501	J1653.8+3945	54682.875–55850.125	28014	0.2
103 (22)	Mkn 501	J1653.8+3945	54906.875–55004.125	2334	0.9
104 (23)	Mkn 501	J1653.8+3945	54912.875–55038.125	3006	1.5
105 (24)	Mkn 501	J1653.8+3945	54937.875–54955.125	414	3.7
106 (25)	Mkn 501	J1653.8+3945	54937.875–54955.125	414	2.9
107 (26)	Mkn 501	J1653.8+3945	54937.875–54955.125	414	1.2
108 (27)	Mkn 501	J1653.8+3945	54951.875–54955.125	78	0.6
109 (28)	Mkn 501	J1653.8+3945	54972.875–54974.125	30	0.6
110 (29)	Mkn 501	J1653.8+3945	55850.875–55887.125	870	1.2
113 (32)	Mkn 501	J1653.8+3945	56031.875–56033.125	30	0.2
124 (43)	Mkn 501	J1653.8+3945	56086.875–56088.125	30	1.0
126 (45)	Mkn 501	J1653.8+3945	56093.875–56095.125	30	0.0
129 (48)	Mkn 501	J1653.8+3945	56395.054–56395.348	7	0.0
131 (50)	Mkn 501	J1653.8+3945	56421.017–56421.334	8	0.0
165 (10)	1ES 1959+650	J2000.0+6508	56033.875–56079.125	1086	1.1
166 (11)	1ES 1959+650	J2000.0+6508	56066.875–56068.125	30	0.0
167 (12)	1ES 1959+650	J2000.0+6508	57331.875–57344.125	294	2.6
170 (15)	1ES 1959+650	J2000.0+6508	57552.875–57554.125	30	0.3
171 (16)	1ES 1959+650	J2000.0+6508	57569.875–57571.125	30	1.0
173 (1)	AP Librae	J1517.7−2422	55325.875–55689.125	8718	1.5
174 (1)	PKS 0625−354	J0627.0−3529	56231.875–56292.125	1446	0.2
176 (2)	I Zw 187	J1728.3+5013	57306.875–57328.125	510	0.1
179 (2)	BL Lacertae	J2202.7+4216	55739.375–55740.625	30	0.0
180 (3)	BL Lacertae	J2202.7+4216	57187.875–57201.125	318	0.6
181 (4)	BL Lacertae	J2202.7+4216	57187.875–57189.125	30	1.8
182 (5)	BL Lacertae	J2202.7+4216	57666.039–57666.416	9	0.3
187 (5)	PKS 2005-489	J2009.4−4849	54972.875–55014.125	990	0.2
191 (1)	S3 1741+19	J1744.0+1935	55295.875–55707.125	9870	0.4
209 (15)	PKS 2155−304	J2158.8−3013	56402.875–56601.125	4758	0.2
210 (16)	PKS 2155−304	J2158.8−3013	56804.875–56817.125	294	1.4
215 (3)	H 1426+428	J1428.5+4240	55196.875–56657.125	35046	2.1
216 (1)	B2 1215+30	J1217.9+3007	55561.875–55600.125	918	0.7
218 (3)	B2 1215+30	J1217.9+3007	56900.875–57234.125	7998	1.5
220 (5)	B2 1215+30	J1217.9+3007	57265.875–57600.125	8022	1.9
222 (7)	B2 1215+30	J1217.9+3007	57631.875–57965.125	7998	1.5
226 (2)	1ES 0806+524	J0809.8+5218	55567.875–55623.125	1326	0.0
227 (3)	1ES 0806+524	J0809.8+5218	55615.875–55617.125	30	0.0
228 (1)	PKS 1440−389	J1443.9−3908	55984.875–56074.125	2142	0.6
232 (4)	1ES 0229+200	J0232.8+2018	55926.875–57387.125	35046	1.2
242 (3)	PG 1218+304	J1221.3+3010	54800.875–54952.125	3630	1.1
245 (1)	1E 0317.0+1835	J0319.8+1845	54731.875–55485.125	18078	0.8
248 (3)	1ES 1011+496	J1015.0+4926	55609.875–56070.125	11046	1.5
249 (4)	1ES 1011+496	J1015.0+4926	56693.875–56723.125	702	0.6
252 (1)	PKS 1510−089	J1512.8−0906	54909.875–54918.125	198	0.1
256 (5)	PKS 1510−089	J1512.8−0906	57538.875–57539.125	6	0.6
262 (1)	4C +21.35	J1224.9+2122	55364.783–55365.056	7	0.4
265 (1)	B2 1420+32	J1422.3+3223	58868.175–58870.425	54	0.9
266 (1)	PKS 1441+25	J1443.9+2501	57129.875–57135.625	138	1.7
267 (2)	PKS 1441+25	J1443.9+2501	57132.875–57140.125	174	0.9
268 (3)	PKS 1441+25	J1443.9+2501	57135.375–57139.625	102	0.8

Appendix C
Reconstructed EBL Intensities and Covariance Matrix

We report in Table 3 the EBL intensities obtained by applying the Bayesian framework discussed in this work to the γ-ray data from STeVECat and the contemporaneous Fermi-LAT observations. We report in Table 4 the correlation matrix associated to these intensities.

Table 3
Reconstructed EBL Intensities at Redshift $z = 0$

	λ (μm)	$\lambda_{\rm min}$ (μm)	$\lambda_{\rm max}$ (μm)	$\nu I_\nu(\lambda)$ (nW m^{-2} sr^{-1})
1	0.27	0.18	0.40	4.9 ± 3.9
2	0.60	0.40	0.90	6.9 ± 1.9
3	1.35	0.90	2.02	10.9 ± 1.3
4	3.04	2.02	4.56	7.9 ± 0.9
5	6.83	4.56	10.3	3.1 ± 0.7
6	15.4	10.3	23.1	3.8 ± 0.9
7	34.6	23.1	51.9	5.1 ± 1.3
8	77.8	51.9	117	6.2 ± 2.1

Table 4
Correlation Matrix of the Different EBL Intensities Reconstructed in This Work

1	2	3	4	5	6	7	8
1.00	0.11	0.19	0.01	−0.22	−0.13	−0.13	−0.18
⋯	1.00	0.46	0.37	0.02	−0.14	−0.02	−0.01
⋯	⋯	1.00	0.51	0.47	−0.13	−0.15	−0.02
⋯	⋯	⋯	1.00	0.57	0.24	−0.05	−0.02
⋯	⋯	⋯	⋯	1.00	0.64	0.43	0.12
⋯	⋯	⋯	⋯	⋯	1.00	0.67	0.39
⋯	⋯	⋯	⋯	⋯	⋯	1.00	0.55
⋯	⋯	⋯	⋯	⋯	⋯	⋯	1.00

ORCID iDs

Lucas Gréaux https://orcid.org/0000-0003-0627-8436
Jonathan Biteau https://orcid.org/0000-0002-4202-8939
Mireia Nievas Rosillo https://orcid.org/0000-0002-8321-9168

References

Abdollahi, S., Acero, F., Baldini, L., et al. 2022, ApJS, 260, 53
Abeysekara, A. U., Archer, A., Benbow, W., et al. 2019, ApJ, 885, 150
Acciari, V. A., Ansoldi, S., Antonelli, L. A., et al. 2019, MNRAS, 486, 4233
Ackermann, M., Ajello, M., Allafort, A., et al. 2012, Sci, 338, 1190
Aharonian, F., Akhperjanian, A. G., Bazer-Bachi, A. R., et al. 2007, ApJL, 664, L71
Aleksić, J., Ansoldi, S., Antonelli, L. A., et al. 2016, APh, 72, 61
Andrews, S. K., Driver, S. P., Davies, L. J. M., Lagos, C. d. P., & Robotham, A. S. G. 2017a, MNRAS, 474, 898
Andrews, S. K., Driver, S. P., Davies, L. J. M., et al. 2017b, MNRAS, 470, 1342
Ashton, T., Backes, M., Balzer, A., et al. 2020, APh, 118, 102425
Atwood, W. B., Abdo, A. A., Ackermann, M., et al. 2009, ApJ, 697, 1071
Bernal, J. L., Sato-Polito, G., & Kamionkowski, M. 2022, PhRvL, 129, 231301
Bernstein, R. A. 2007, ApJ, 666, 663
Biasuzzi, B., Hervet, O., Williams, D. A., & Biteau, J. 2019, A&A, 627, A110
Biteau, J. 2023, The Multi-Messenger Extragalactic Spectrum, v1.0, Zenodo, doi:1010.5281/zenodo.7842239
Biteau, J., & Meyer, M. 2022, Galax, 10, 39
Biteau, J., & Williams, D. A. 2015, ApJ, 812, 60
Cao, Z., Aharonian, F., An, Q., et al. 2023, SciA, 9, eadj2778
Cheng, A. F., Weaver, H. A., Conard, S. J., et al. 2008, SSRv, 140, 189
Cheng, Y.-T., Arai, T., Bangale, P., et al. 2021, ApJ, 919, 69
Conselice, C. J., Wilkinson, A., Duncan, K., & Mortlock, A. 2016, ApJ, 830, 83
Cooray, A. 2016, RSOS, 3, 150555
Cooray, A., Gong, Y., Smidt, J., & Santos, M. G. 2012a, ApJ, 756, 92
Cooray, A., Smidt, J., de Bernardis, F., et al. 2012b, Natur, 490, 514
CTA Consortium 2021, JCAP, 2021, 048
Desai, A., Helgason, K., Ajello, M., et al. 2019, ApJ, 874, L7
Domínguez, A., Østergaard Kirkeberg, P., Wojtak, R., et al. 2024, MNRAS, 527, 4632
Domínguez, A., & Prada, F. 2013, ApJL, 771, L34
Domínguez, A., Wojtak, R., Finke, J., et al. 2019, ApJ, 885, 137
Driver, S. P. 2021, arXiv:2102.12089
Driver, S. P., Andrews, S. K., Davies, L. J., et al. 2016, ApJ, 827, 108
Driver, S. P., Bellstedt, S., Robotham, A. S. G., et al. 2022, MNRAS, 513, 439
Euclid Collaboration, Mellier, Y., Abdurro'uf, et al. 2024, arXiv:2405.13491
Fermi-LAT Collaboration 2018, Sci, 362, 1031
Fermi Science Support Development Team 2019, Fermitools: Fermi Science Tools, Astrophysics Source Code Library, ascl:1905.011
Foreman-Mackey, D., Hogg, D. W., Lang, D., & Goodman, J. 2013, PASP, 125, 306
Franceschini, A., Rodighiero, G., & Vaccari, M. 2008, A&A, 487, 837
Gilmore, R. C., Somerville, R. S., Primack, J. R., & Domínguez, A. 2012, MNRAS, 422, 3189
Goldoni, P. 2021, Review of Redshift Values of Bright AGNs with Hard Spectra in 4LAC catalog, v2, Zenodo, doi:10.5281/zenodo.5512660
Gould, R. J., & Schréder, G. P. 1967, PhRv, 155, 1408
Gréaux, L., Biteau, J., Hassan, T., et al. 2023a, ICRC (Nagoya), 444, 751
Gréaux, L., Biteau, J., Hassan, T., et al. 2023b, STeVECat, the Spectral TeV Extragalactic Catalog, v1, Zenodo, doi:10.5281/ZENODO.8152245
Hauser, M. G., & Dwek, E. 2001, ARA&A, 39, 249
H.E.S.S. Collaboration, Abdalla, H., Abramowski, A., et al. 2017, A&A, 606, A59
H.E.S.S. Collaboration, Abramowski, A., Acero, F., et al. 2013, A&A, 550, A4
Holder, J., Atkins, R. W., Badran, H. M., et al. 2006, APh, 25, 391
Ivezić, Ž., Kahn, S. M., Tyson, J. A., et al. 2019, ApJ, 873, 111
Kawara, K., Matsuoka, Y., Sano, K., et al. 2017, PASJ, 69, 31
Kneiske, T. M., Mannheim, K., & Hartmann, D. H. 2002, A&A, 386, 1
Koushan, S., Driver, S. P., Bellstedt, S., et al. 2021, MNRAS, 503, 2033
Kramer, D. M., Carleton, T., Cohen, S. H., et al. 2022, ApJL, 940, L15
Lauer, T. R., Postman, M., Spencer, J. R., et al. 2022, ApJL, 927, L8
Lauer, T. R., Postman, M., Weaver, H. A., et al. 2021, ApJ, 906, 77
Matsumoto, T., & Tsumura, K. 2019, PASJ, 71, 88
Matsuura, S., Arai, T., Bock, J. J., et al. 2017, ApJ, 839, 7
Mattila, K., & Väisänen, P. 2019, ConPh, 60, 23
Nakayama, K., & Yin, W. 2022, PhRvD, 106, 103505
Nigro, C., Deil, C., Zanin, R., et al. 2019, A&A, 625, A10
Nikishov, A. I. 1961, ZhETF, 41, 549, https://www.osti.gov/biblio/4836265
Planck Collaboration 2020, A&A, 641, A6
Postman, M., Lauer, T. R., Parker, J. W., et al. 2024, ApJ, 972, 95
Raue, M., & Mazin, D. 2008, IJMPD, 17, 1515
Riess, A. G., Yuan, W., Macri, L. M., et al. 2022, ApJL, 934, L7
Saldana-Lopez, A., Domínguez, A., Pérez-González, P. G., et al. 2021, MNRAS, 507, 5144
Sanchez, D., & Deil, C. 2015, Enrico: Python package to simplify Fermi-LAT analysis, Astrophysics Source Code Library, ascl:1501.008
Stecker, F. W., de Jager, O. C., & Salamon, M. H. 1992, ApJL, 390, L49
Symons, T., Zemcov, M., Cooray, A., Lisse, C., & Poppe, A. R. 2023, ApJ, 945, 45
Weaver, H. A., Cheng, A. F., Morgan, F., et al. 2020, PASP, 132, 035003
Windhorst, R. A., Carleton, T., O'Brien, R., et al. 2022, AJ, 164, 141
Windhorst, R. A., Cohen, S. H., Jansen, R. A., et al. 2023, AJ, 165, 13
Zemcov, M., Smidt, J., Arai, T., et al. 2014, Sci, 346, 732